JOURNAL OF COMPUTATIONAL PHYSICS **125,** 513–525 (1996)
ARTICLE NO. 0112

A Three-Dimensional Plasma–Neutral Gas–Fluid Code

G. T. BIRK* AND A. OTTO†

*Ruhr-Universität Bochum, Theoretische Physik IV, Universitaetsstrasse 150, 44780 Bochum, Germany and †Geophysical Institute, University of Alaska, PO Box 757320, Fairbanks, Alaska 99775

Received June 1, 1995; revised November 20, 1995

Macroscopic dynamics of interacting hot plasmas and partially ionized gases can be studied by means of fluid simulations. Important applications are the Earth's magnetosphere–ionosphere–thermosphere system and the interaction of solar photospheric and coronal plasma. We developed a quasi-neutral compressible 3D fluid code that integrates the closed set of balance equations for the plasma fluid, the neutral gas, and the magnetic flux. We derived a quite general set of dimensionless balance equations taking into account mass, momentum and energy conservation. For a number of applications in partially ionized space plasmas the equations can be reduced to numerically tractable equations. The kernel of the numerical algorithm is the leapfrog method which is of second-order accuracy in space and time. The code was tested by simulating characteristic wave and instability phenomena.

1. INTRODUCTION

Investigations on nonlinear dynamic processes of partially ionized space plasmas are greatly supported by computer simulations. Important applications for a plasma–neutral gas code; e.g., are dynamic phenomena associated with solar prominences, molecular clouds, the interaction of HI- and HII-regions, transient phenomena at the Venus ionopause, cometary plasmas, and, in particular, the coupled magnetosphere–ionosphere–thermosphere system of the Earth. In laboratory plasmas, e.g., in fusion plasmas the plasma–neutral gas interaction is also of importance. Several numerical approaches deal with impurity effects and neutral beam heating in laboratory plasmas, e.g., by solving the Fokker–Planck equation by means of the Galerkin method [1], propagators for the equations of transport theory [2] or by integrating reduced fluid equations under the assumption of ambipolarity [3]. Recently, a simplified two-dimensional fluid code that allows to study shock phenomena has been introduced [4], as well as a two-dimensional fluid code that includes ion neutral drag, recombination, the Hall term, and gravitation, but no energy equations [5, 6].

In this paper we present a 3D cartesian plasma–neutral gas fluid code. It is based on the integration of the balance equations for the plasma and neutral gas quantities and the magnetic field. The basic equations are derived under the constraints of conservation of mass, momentum, and energy. The transport coefficients are chosen semi-empirically as functions of temperature and mass density. We do not account for a self-consistent treatment of the kinetic processes (collisions, ionization, and recombination). However, combination with a kinetic treatment can result in a fully self-consistent modeling of transport phenomena. In the numerical code presented, ionization and recombination are included in a straightforward manner, as well as momentum transfer between neutrals and plasma particles and collisional thermalization. The discretization of the balance equations for the plasma and the neutral gas fluid is based on the leapfrog algorithm, e.g., [7]. We choose a semi-implicit formulation of the discretized induction equation that allows for including the Hall term, the convective and the dissipative terms, as well as electron pressure. The balance equations for the internal energies are formulated as equations for the pressures. They include dissipative and thermalization terms, as well as source terms that are chosen in a way to guarantee energy conservation. Besides the equations for the plasma and the neutral gas pressure, an equation for the electron pressure is incorporated to close the equation system.

In the following section the basic equations are derived in a convenient normalization. The equations are reduced to numerically tractable equations on grounds of physically motivated assumptions and approximations. In Section 3 we present quantitative tests of the code to prove its reliability. We sum up our findings in Section 4.

2. MODEL EQUATIONS AND THE INTEGRATION SCHEME

2.1. *Derivation of the Balance Equations*

To derive the quasi-neutral plasma and neutral gas fluid equations we have to start from the balance equations for mass, momentum and internal energy density of the electrons, ions, and neutrals

0021-9991/96 $18.00

$$\frac{\partial \rho_\alpha}{\partial t} = -\nabla \cdot (\rho_\alpha \mathbf{v}_\alpha) + Q_\alpha^c \tag{1}$$

$$\frac{\partial}{\partial t}(\rho_\alpha \mathbf{v}_\alpha) = -\nabla \cdot (\rho_\alpha \mathbf{v}_\alpha \mathbf{v}_\alpha) - \nabla \cdot \mathbf{P}_\alpha + \mathbf{F}_\alpha + \mathbf{v}_\alpha Q_\alpha^c + \mathbf{Q}_\alpha^p \tag{2}$$

$$\frac{\partial}{\partial t}(\rho_\alpha \varepsilon_\alpha) = -\nabla \cdot (\rho_\alpha \varepsilon_\alpha \mathbf{v}_\alpha) - \mathbf{P}_\alpha : \nabla \mathbf{v}_\alpha + Q_\alpha^E, \tag{3}$$

where α denotes the different species. $\rho_\alpha = \sum_s \rho_{\alpha_s}$ is the mass density, where the index s denotes different populations of ions and neutrals. $\mathbf{v}_\alpha$, $\rho_\alpha \varepsilon_\alpha$, and $\mathbf{F}_\alpha$ denote, fluid velocity, internal energy density, and external forces, i.e., the Lorentz force and the gravitational force, respectively. The source terms are defined as moments of the collision integrals,

$$Q_\alpha^c = m_\alpha \int d\mathbf{u}_\alpha \left[\frac{\partial f_\alpha}{\partial t}\right]_{c_p} \tag{4}$$

$$\mathbf{Q}_\alpha^p = m_\alpha \int d\mathbf{u}_\alpha (\mathbf{u}_\alpha - \mathbf{v}_\alpha) \left[\frac{\partial f_\alpha}{\partial t}\right]_{c_p} \tag{5}$$

$$Q_\alpha^E = \frac{m_\alpha}{2} \int d\mathbf{u}_\alpha (\mathbf{u}_\alpha - \mathbf{v}_\alpha)(\mathbf{u}_\alpha - \mathbf{v}_\alpha) \left[\frac{\partial f_\alpha}{\partial t}\right]_{c_e}, \tag{6}$$

where f_α is the one-particle distribution function in phase space of species α and $\mathbf{u}_\alpha$ is the one-particle velocity. In the following, we neglect the effects of viscosity. Thus the pressure tensors

$$\mathbf{P}_\alpha = m_\alpha \int d\mathbf{u}_\alpha (\mathbf{u}_\alpha - \mathbf{v}_\alpha)(\mathbf{u}_\alpha - \mathbf{v}_\alpha) f_\alpha \tag{7}$$

reduces to

$$p_\alpha = \tfrac{1}{3} \mathrm{Tr}(\mathbf{P}_\alpha). \tag{8}$$

In order to guarantee mass, momentum, and energy conservation the source terms have to satisfy the equations:

$$\sum_\alpha Q_\alpha^c = 0 \tag{9}$$

$$\sum_\alpha (Q_\alpha^c \mathbf{v}_\alpha + \mathbf{Q}_\alpha^p) = 0 \tag{10}$$

$$\sum_\alpha (\tfrac{1}{2} Q_\alpha^c v_\alpha^2 + \mathbf{Q}_\alpha^p \cdot \mathbf{v}_\alpha + Q_\alpha^E) = 0. \tag{11}$$

To derive the quasi-neutral plasma equations that allow for a unified treatment of the electron and the ion fluid, we have to calculate the following expressions:

(a) $\frac{\partial}{\partial t}(\rho_e + \rho_i)$

(b) $\frac{\partial}{\partial t}(\rho_e v_e + \rho_i v_i)$

(c) $\frac{\partial}{\partial t}(p_e + p_i)$

(d) $m_e \frac{\partial}{\partial t}(\rho_i \mathbf{v}_i) - m_i \frac{\partial}{\partial t}(\rho_e \mathbf{v}_e)$,

where we make use of the relations

$$n_e = n_i = n, \quad \rho = n(m_e + m_i), \quad p = p_e + p_i$$

$$\rho \mathbf{v} = \rho_e \mathbf{v}_e + \rho_i \mathbf{v}_i$$

$$\mathbf{v}_i = \mathbf{v} + \frac{m_e}{e\rho}\mathbf{j}, \quad \mathbf{v}_e = \mathbf{v} - \frac{m_i}{e\rho}\mathbf{j},$$

where n, n_e, and n_i denote the particle densities. The indices e and i denote the electrons and ions. Plasma variables are represented by symbols without index.

The continuity equation for the plasma fluid is given by

$$\frac{\partial \rho}{\partial t} = -\nabla \cdot (\rho \mathbf{v}) + Q^c \tag{12}$$

with $Q^c = Q_e^c + Q_i^c$, where Q_e^c and Q_i^c are the source terms of the respective electron and ion continuity equations. With $\mathbf{Q}^p = \mathbf{Q}_e^p + \mathbf{Q}_i^p$ summation of the momentum balance equations of the charged species gives

$$\frac{\partial}{\partial t}(\rho \mathbf{v}) = -\nabla \cdot (\rho \mathbf{v}\mathbf{v}) - \frac{m_i m_e}{e^2} \nabla \cdot \left(\frac{1}{\rho}\mathbf{j}\mathbf{j}\right) - \nabla p + \frac{1}{c}\mathbf{j} \times \mathbf{B} + \rho \mathbf{g} + Q^c \mathbf{v} + \mathbf{Q}^p, \tag{13}$$

where $\mathbf{g}$ denotes the gravitational acceleration. Ohm's law is given by

$$\mathbf{E} + \frac{1}{c}\mathbf{v} \times \mathbf{B} = \frac{m_e m_i}{e^2 \rho}\left(\frac{\partial \mathbf{j}}{\partial t} + \nabla \cdot (\mathbf{v}\mathbf{j} + \mathbf{j}\mathbf{v})\right) + \frac{m_e m_i}{e^3 \rho} \nabla \cdot \left(\frac{1}{\rho}\,\mathbf{j}\mathbf{j}\right) + \frac{1}{e\rho}\nabla(m_e p_i - m_i p_e) - \frac{m_e - m_i}{ce\rho}\mathbf{j} \times \mathbf{B} - \frac{m_e m_i \mathbf{j}}{e^2 \rho^2} Q^c - \frac{m_i - m_e}{e\rho}\mathbf{Q}^p + \frac{1}{e\rho}(m_e \mathbf{Q}_e^p - m_i \mathbf{Q}_i^p). \tag{14}$$

With the definition $\varepsilon_\alpha = (1/\gamma_\alpha - 1)(p_\alpha/\rho_\alpha)$, summation of the internal energy density equations for electrons and ions gives

$$\frac{1}{\gamma-1}\frac{\partial p}{\partial t} = -\frac{1}{\gamma-1}\nabla\cdot(p\mathbf{v}) - p\nabla\cdot\mathbf{v} - \frac{1}{\gamma-1}\nabla\cdot\left(\frac{m_e p_i - m_i p_e}{e\rho}\mathbf{j}\right) - \frac{p_i m_e - p_e m_i}{e}\nabla\cdot\frac{\mathbf{j}}{\rho} + Q^E \tag{15}$$

with $Q^E = Q_e^E + Q_i^E$ and $\gamma_e = \gamma_i = \gamma$. The equation for the electron pressure reads

$$\frac{1}{\gamma-1}\frac{\partial p_e}{\partial t} = -\frac{1}{\gamma-1}\nabla\cdot(p_e\mathbf{v}_e) - p_e\nabla\cdot\mathbf{v}_e + Q_e^E. \tag{16}$$

Heat conduction is neglected in both energy equations.

The hydrodynamic equations for the neutral gas fluid are given by

$$\frac{\partial\rho_n}{\partial t} = -\nabla\cdot(\rho_n\mathbf{v}_n) + Q_n^c \tag{17}$$

$$\frac{\partial}{\partial t}(\rho_n\mathbf{v}_n) = -\nabla\cdot(\rho_n\mathbf{v}_n\mathbf{v}_n) - \nabla p_n + \rho_n\mathbf{g} + \mathbf{v}_n Q_n^c + \mathbf{Q}_n^p \tag{18}$$

$$\frac{1}{\gamma_n-1}\frac{\partial p_n}{\partial t} = -\frac{1}{\gamma_n-1}\nabla\cdot(p_n\mathbf{v}_n) - p_n\nabla\cdot\mathbf{v}_n + Q_n^E. \tag{19}$$

Again heat conduction, as well as changes in internal energy due to gravitational forces were neglected.

The source terms of the balance equations can be defined with the help of the source terms of the equations for the velocity moments of the three different species. These can be found in the literature, e.g., [8, 9]. We note that the required evaluation of the collision integrals is very difficult and is only possible under certain assumptions (e.g., velocity independent collision frequencies). For our purposes it is sufficient to determine the macroscopic effects of ionization and recombination as well as inelastic and elastic collisions between charged and neutral particles, taking into account the respective laws of conservation.

As source terms of the continuity equations we choose (cf. [8])

$$Q^c = (\iota - \beta\rho)\rho, \quad Q_n^c = -(\iota - \beta\rho)\rho, \tag{20}$$

where ι denotes the ionization frequency and β is the recombination coefficient.

The momentum transfer between the plasma and the neutral gas is a linear function of the difference of the velocities of the respective fluids. The source terms of the momentum balance equations of the three species are given by (cf. [9])

$$\mathbf{Q}_{e_{i,n}}^p = \rho_e\nu_{ei}(\mathbf{v}_i - \mathbf{v}_e) + \rho_e\nu_{en}(\mathbf{v}_n - \mathbf{v}_e) \tag{21}$$

$$\mathbf{Q}_{e_{i,n}}^p = \rho_i\nu_{ie}(\mathbf{v}_e - \mathbf{v}_i) + \rho_i\nu_{in}(\mathbf{v}_n - \mathbf{v}_i) \tag{22}$$

$$\mathbf{Q}_{n_{e,i}}^p = \rho_n\nu_{ne}(\mathbf{v}_e - \mathbf{v}_n) + \rho_n\nu_{ni}(\mathbf{v}_i - \mathbf{v}_n), \tag{23}$$

where the ν's denote the effective elastic collision frequencies between the electrons, ions, and neutrals. We do not consider inelastic resonant collisions.

Neglecting terms of the order of $(m_e/m_i)\mathbf{j}$ we get the momentum source terms

$$\mathbf{Q}^p = -(\nu_{12}^S + \nu_{12}^A)\rho(\mathbf{v} - \mathbf{v}_n) \tag{24}$$

$$\mathbf{Q}_n^p = -(\nu_{21}^S + \nu_{21}^A)\rho_n(\mathbf{v}_n - \mathbf{v}) \tag{25}$$

with

$$\nu_{12}^S = \frac{m_i\nu_{in} + m_e\nu_{en}}{m_e + m_i}, \quad \nu_{12}^S\rho = \nu_{21}^S\rho_n, \tag{26}$$

and

$$\nu_{12}^A = 2(\iota - \beta\rho) + \frac{\rho_n}{\rho}\nu_{21}^A \tag{27}$$

to guarantee momentum conservation.

In deriving the source terms of the energy equations we have to take care about conservation of the total energy that requires

$$\left(\frac{1}{2}v^2 + \frac{m_e m_i}{e^2\rho^2}j^2\right)Q^c + \frac{1}{2}v_n^2 Q_n^c + \mathbf{Q}^p\cdot\mathbf{v} + \mathbf{Q}_n^p\cdot\mathbf{v}_n + \frac{m_e}{e\rho}\mathbf{Q}_i^p\cdot\mathbf{j} - \frac{m_i}{e\rho}\mathbf{Q}_e^p\cdot\mathbf{j} + Q^E + Q_n^E = 0. \tag{28}$$

The energy source terms Q^E and Q_n^E have to include thermalization (Q^{E^T}, $Q_n^{E^T}$), as well as energy changes due to momentum transfer by collisions (Q^{E^p}, $Q_n^{E^p}$) and by ionization/recombination (Q^{E^c}, $Q_n^{E^c}$). Obviously, a complete, exact treatment would result in balance equations for the internal energies that would not allow for numerical treatment at all. Nevertheless, we can derive source terms that include the main physical effects for the macroscopic processes under consideration by making use of rational assumptions and approximations. We derive the source terms Q^E and Q_n^E from the energy source terms of each species (cf. [9]):

$$\mathbf{Q}^{E}_{e_{i,n}} = \frac{3m_e\nu_{ei}}{m_e+m_i}(p_i-p_e) + \frac{3m_e\nu_{en}}{m_e+m_n}\left(\frac{n}{n_n}p_n - p_e\right) + \frac{\rho_e m_i \nu_{ei}}{m_e+m_i}(\mathbf{v}_e-\mathbf{v}_i)^2 + \frac{\rho_e m_n \nu_{en}}{m_e+m_n}(\mathbf{v}_e-\mathbf{v}_n)^2 + Q_e^{E^c} \tag{29}$$

$$\mathbf{Q}^{E}_{i_{e,n}} = \frac{3m_i\nu_{ie}}{m_e+m_i}(p_e-p_i) + \frac{3m_i\nu_{in}}{m_i+m_n}\left(\frac{n}{n_n}p_n - p_i\right) + \frac{\rho_i m_e \nu_{ie}}{m_e+m_i}(\mathbf{v}_i-\mathbf{v}_e)^2 + \frac{\rho_i m_n \nu_{in}}{m_i+m_n}(\mathbf{v}_i-\mathbf{v}_n)^2 + Q_i^{E^c} \tag{30}$$

$$\mathbf{Q}^{E}_{n_{e,i}} = \frac{3m_n\nu_{ne}}{m_e+m_n}\left(\frac{n_n}{n}p_e - p_n\right) + \frac{3m_n\nu_{ni}}{m_i+m_n}\left(\frac{n_n}{n}p_i - p_n\right) + \frac{\rho_n m_e \nu_{ne}}{m_e+m_n}(\mathbf{v}_n-\mathbf{v}_e)^2 + \frac{\rho_n m_i \nu_{ni}}{m_i+m_n}(\mathbf{v}_n-\mathbf{v}_i)^2 + Q_n^{E^c}, \tag{31}$$

where we neglected the release of gravitational energy.

Assuming that the neutral gas temperature does not directly change due to ionization/recombination, the simple expressions for Q^{E^c} and $Q_n^{E^c}$ are given by

$$Q^{E^c} = \tfrac{3}{2}(\iota-\beta\rho)\frac{\rho}{\rho_n}p_n + \tfrac{1}{2}(\iota-\beta\rho)(\mathbf{v}-\mathbf{v}_n)^2 \tag{32}$$

$$Q_n^{E^c} = -\tfrac{3}{2}(\iota-\beta\pi)\frac{\rho}{\rho_n}p_n, \tag{33}$$

where we neglected terms of the order of $(m_e/m_i)j^2$. With Eq. (32) and Eq. (33) and the expressions gained for the energy source terms of each species Eq. (29)–(31), we get the energy source terms for the plasma and the neutral gas fluid,

$$Q^E = -3\nu_{12}^S\left(p - \frac{\rho}{\rho_n}p_n\right) + \eta j^2 + \tfrac{3}{2}(\iota-\beta\rho)\frac{\rho}{\rho_n}p_n + \tfrac{1}{2}\rho(3\nu_{12}^S + \iota - \beta\rho)(\mathbf{v}-\mathbf{v}_n)^2 \tag{34}$$

$$Q_n^E = -3\nu_{21}^S\left(p_n - \frac{\rho_n}{\rho}p\right) - \tfrac{3}{2}(\iota+\beta\rho)\frac{\rho}{\rho_n}p_n + \tfrac{3}{2}\rho_n\nu_{21}^S(\mathbf{v}_n-\mathbf{v})^2, \tag{35}$$

where we neglected terms of the order of m_e/m_i and $(m_e/m_i)\mathbf{jv}$. The resistivity η is defined by $\eta = (m_e^2/e^2\rho_e)(\nu_{ei} + \nu_{en} + \iota - \beta\rho)$. For our choice of the energy source terms Eq. (34) and Eq. (35) total energy conservation (cf. Eq. (28)) requires

$$\nu_{21}^A = \frac{\rho(\iota-\beta\rho)(v^2 - \mathbf{v}\cdot\mathbf{v}_n)}{\rho_n(2\mathbf{v}_n\mathbf{v} - v^2 - v_n^2)}. \tag{36}$$

Before collecting the plasma and neutral gas fluid equations as incorporated in our code it might be useful to sum up the main assumptions needed to derive these equations:

1. Quasineutrality
2. Neglecting terms of the order of m_e/m_i, $(m_e/m_i)\mathbf{j}$, $\nabla\cdot((1/\rho)\mathbf{jj})$, and $(m_e/m_i)\mathbf{jv}$
3. Neglecting electron inertia terms
4. Comparable ion and electron temperatures
5. Neglecting heat conduction and the release of gravitational energy as a heat source
6. Ideal gases.

A convenient normalization of the transport equations for plasmas with comparable diffusion time, Alfvénic transit time, and collision time read as follows: Length scales are normalized to a characteristic length scale L_0 of the system, ρ to the mass density $\rho_0 = m_0 n_0$ (m_0 is the typical ion mass and n_0 is the number density), $\mathbf{B}$ to a typical value B_0 of the magnetic field, p to $P_0 = B_0^2/8\pi$, $\mathbf{v}$ to the typical Alfvén velocity $V_A = B_0/\sqrt{4\pi\rho_0}$, and $\mathbf{j}$ to $cB_0/(4\pi L_0)$. The time scale is normalized to the Alfvénic transit time $\tau_A = L_0/V_A$.

Thus, the dimensionless fluid equations are given by:

$$\frac{\partial\rho}{\partial t} = -\nabla\cdot(\mathbf{v}\rho) + \iota\rho - \beta\rho^2 \tag{37}$$

$$\frac{\partial\rho_n}{\partial t} = -\nabla\cdot(\mathbf{v}_n\rho_n) - \iota\rho + \beta\rho^2 \tag{38}$$

$$\frac{\partial}{\partial t}(\rho\mathbf{v}) = -\nabla\cdot(\rho\mathbf{v}\mathbf{v}) - \tfrac{1}{2}\nabla p + (\nabla\times\mathbf{B})\times\mathbf{B} + \rho\mathbf{g} + \rho\mathbf{v}(\iota-\beta\rho) - \rho(\nu_{12}^A + \nu_{12}^S)(\mathbf{v}-\mathbf{v}_n) \tag{39}$$

$$\frac{\partial}{\partial t}(\rho_n\mathbf{v}_n) = -\nabla\cdot(\rho_n\mathbf{v}_n\mathbf{v}_n) - \tfrac{1}{2}\nabla p_n + \rho_n\mathbf{g} - \rho\mathbf{v}_n(\iota-\beta\rho) - \rho_n(\nu_{21}^A + \nu_{21}^S)(\mathbf{v}_n-\mathbf{v}) \tag{40}$$

$$\frac{\partial\mathbf{B}}{\partial t} = \nabla\times\left(\frac{1}{ne}\nabla p_e\right) + \nabla\times(\mathbf{v}\times\mathbf{B}) - \nabla\times\left(\frac{1}{ne}(\nabla\times\mathbf{B})\times\mathbf{B}\right) - \nabla\times(\eta\nabla\times\mathbf{B}) \tag{41}$$

$$\frac{\partial p}{\partial t} = -\mathbf{v}\cdot\nabla p - \gamma p\nabla\cdot\mathbf{v} + (\gamma-1)\left(2\eta(\nabla\times\mathbf{B})^2 + (\iota-\beta\rho)\frac{\rho}{\rho_n}p_n - 3\nu_{12}^S\left(p - \frac{\rho}{\rho_n}p_n\right) + \rho(\nu_{12}^S + \iota - \beta\rho)(v-v_n)^2\right) \tag{42}$$

$$\frac{\partial p_e}{\partial t} = -\mathbf{v}_e \cdot \nabla p_e - \gamma p_e \nabla \cdot \mathbf{v}_e + (\gamma - 1)\left(2\eta(\nabla \times \mathbf{B})^2 + \tfrac{1}{2}(\iota - \beta\rho)\frac{\rho}{\rho_n} p_n\right) \quad (43)$$

$$\frac{\partial p_n}{\partial t} = -\mathbf{v}_n \cdot \nabla p_n - \gamma_n p_n \nabla \cdot \mathbf{v}_n - (\gamma_n - 1)\left(3\eta_{21}^S\left(p_n - \frac{\rho_n}{\rho} p\right) + (\iota - \beta\rho)\frac{\rho}{\rho_n} p_n - \rho_n \nu_{21}^S (\mathbf{v}_n - v)^2\right) \quad (44)$$

2.2. *Numerical Realization and Discretization Scheme*

The plasma-neutral gas code presented in this paper is a further development of a 3D resistive MHD code [10] the reliability of which has been proved in many applications to space plasma phenomena, e.g., [11–13]. The balance equations for mass density, momentum density, and energy density are discretized on the grounds of the leapfrog algorithm with second-order accuracy in space and time (cf. [7]). This algorithm has to be modified in order to include the source terms due to plasma-neutral gas interaction.

The explicit finite difference method employed in the code allows for the use of a nonuniform spatial grid. Without this the nonlinear dynamics of plasma processes operating on different spatial scales could not properly be simulated. Moreover, this method allows for a high degree of vectorization. In particular, two dimensions of the spatial grid have been rearranged into a single one-dimensional array to gain a significant speedup using vector computers. The source terms are taken into account in the following way. First, the respective discretized transport equation is integrated a half time step. This integration is followed by a second integration of a half time step, but this time we use a corrected flux transport of the source term,

$$Q(t + \tfrac{1}{2}) = Q(t - 1) - \Delta t(C(t) - S(t)) \quad (45a)$$

$$Q(t + 1) = Q(t + \tfrac{1}{2}) - \Delta t(C(t) - S(t) + S(t) - S(t + \tfrac{1}{2})) \quad (45b)$$

where Q, C, and S denote the transported quantity, the conservatively formulated part of the respective transport equation, and the source term that does not fit the conservative formulation.

For illustration, the two-step integration of the discretized continuity equation for the plasma fluid for constant ionization frequency and recombination coefficient reads

$$\rho_{j,k,l}^{n+1/2} = \rho_{j,k,l}^{n-1} - \Delta t\left[\frac{1}{\Delta x_j}(sx_{j+1,k,l}^n - sx_{j-1,k,l}^n) - \frac{1}{\Delta y_k}(sx_{j,k+1,l}^n - sx_{j,k-1,l}^n) - \frac{1}{\Delta z_l}(sx_{j,k,l+1}^n - sx_{j,k,l-1}^n) - \frac{\iota}{3}(p_x\rho_{j+1,k,l}^n + m_x\rho_{j-1,k,l}^n + p_y\rho_{j,k+1,l}^n + m_y\rho_{j,k-1,l}^n + p_z\rho_{j,k,l+1}^n + m_z\rho_{j,k,l-1}^n) + \frac{\beta}{9}(p_x\rho_{j+1,k,l}^n + m_x\rho_{j-1,k,l}^n + p_y\rho_{j,k+1,l}^n + m_y\rho_{j,k-1,l}^n + p_z\rho_{j,k,l+1}^n + m_z\rho_{j,k,l-1}^n)^2\right] \quad (46a)$$

$$\rho_{j,k,l}^{n+1} = \rho_{j,k,l}^{n+1/2} - \Delta t\left[\frac{1}{\Delta x_j}(sx_{j+1,k,l}^n - sx_{j-1,k,l}^n) - \frac{1}{\Delta y_k}(sx_{j,k+1,l}^n - sx_{j,k-1,l}^n) - \frac{1}{\Delta z_l}(sx_{j,k,l+1}^n - sx_{j,k,l-1}^n) - \iota\rho_{j,k,l}^{n+1/2} + \beta\rho_{j,k,l}^{n+1/2}\rho_{j,k,l}^{n+1/2}\right], \quad (46b)$$

where $sx = \rho v_x$, $sy = \rho v_y$, $sz = \rho v_z$, and $p_x = (x_{j+1} - x_j)/\Delta x_j$ and $m_x = (x_j - x_{j-1})/\Delta x_j$ denote the spatial forward and backward differencing (p_y, m_y, p_z, m_z, accordingly). The symbols Δx, Δy, and Δz denote the spatial differences. The upper indices give the temporal steps and the lower indices give the spatial grid points of the three-dimensional mesh.

This kind of incorporation of the source terms results in a stable algorithm. The collision frequencies and ionization/recombination coefficients can be chosen as constants or as functions of mass density and temperature, respectively. The resistivity can be chosen either constant or depending on the current density. Functional dependence of the resistivity on the current density allows for modeling anomalous dissipation due to microturbulence which probably is of great importance in collisionless space plasmas.

The induction equation is integrated by means of a semi-implicit algorithm (Dufort–Frankel). Under the assumption of constant resistivity, e.g., the x-component of the discretized equation for an equidistant spatial mesh is given by

$$
\begin{aligned}
B^{n+1}_{x_{j,k,l}}\left(1+2\eta\frac{\Delta t}{\Delta x^2+\Delta y^2+\Delta z^2}\right) &= B^{n-1}_{x_{j,k,l}} \\
&+ \frac{2\,\Delta t m}{e\rho\,\Delta y\,\Delta z}\left[p^n_{e_{j,k+1,l}} - p^n_{e_{j,k-1,l}})(\rho^n_{e_{j,k,l+1}} - \rho^n_{e_{j,k,l-1}}\right) \\
&- (p^n_{e_{j,k,l+1}} - p^n_{e_{j,k,l-1}})(\rho^n_{e_{j,k+1,l}} - \rho^n_{e_{j,k-1,l}})] \\
&+ 2\eta\,\Delta t\left[\frac{1}{\Delta x^2}(B^n_{x_{j+1,k,l}} + B^n_{x_{j-1,k,l}})\right. \\
&+ \frac{1}{\Delta y^2}(B^n_{x_{j,k+1,l}} + B^n_{x_{j,k-1,l}}) + \frac{1}{\Delta z^2}(B^n_{x_{j,k,l+1}} + B^n_{x_{j,k,l-1}}) \\
&\left.- \frac{B^n_{x_{j,k,l}}}{\Delta x^2+\Delta y^2+\Delta z^2}\right] \\
&+ \frac{2\,\Delta t}{\Delta y}[(v^n_{x_{j,k+1,l}} + v^n_{ex_{j,k+1,l}} - v^n_{ix_{j,k+1,l}})B^n_{y_{j,k+1,l}} \qquad (47)\\
&- (v^n_{x_{j,k-1,l}} + v^n_{ex_{j,k-1,l}} - v^n_{ix_{j,k-1,l}})B^n_{y_{j,k-1,l}} \\
&- (v^n_{y_{j,k+1,l}} + v^n_{ey_{j,k+1,l}} - v^n_{iy_{j,k+1,l}})B^n_{x_{j,k+1,l}} \\
&- (v^n_{y_{j,k-1,l}} + v^n_{ey_{j,k-1,l}} - v^n_{iy_{j,k-1,l}})B^n_{x_{j,k-1,l}}] \\
&- \frac{2\,\Delta t}{\Delta z}[(v^n_{z_{j,k,l+1}} + v^n_{ez_{j,k,l+1}} - v^n_{iz_{j,k,l+1}})B^n_{x_{j,k,l+1}} \\
&- (v^n_{z_{j,k,l-1}} + v^n_{ez_{j,k,l-1}} - v^n_{iz_{j,k,l-1}})B^n_{x_{j,k,l-1}} \\
&- (v^n_{x_{j,k,l+1}} + v^n_{ex_{j,k,l+1}} - v^n_{ix_{j,k,l+1}})B^n_{z_{j,k,l+1}} \\
&- (v^n_{x_{j,k,l-1}} + v^n_{ex_{j,k,l-1}} - v^n_{ix_{j,k,l-1}}B^n_{z_{j,k,l-1}}].
\end{aligned}
$$

The Hall term was formulated by rewriting the current density $\mathbf{j} = (e\rho/m)(\mathbf{v}_i - \mathbf{v}_e)$. Thus, the Hall term fits the used algorithm (it has the same structure as the convective term). This kind of formulation allows for including the Hall term without making use of complicated semi-implicit algorithms (cf. [14]) in order to suppress numerical instabilities or to allow for reasonable time steps.

The explicit discretization scheme described above and, in particular, the flux-corrected treatment of the source terms allow for a pretty large time step of integration. The linear stability condition is given by the the Courant–Friedrichs–Lewy condition [15] as in the case for the leapfrog algorithm [7]. This condition implies $\Delta t \le \Delta_{\min}/c_{\mathrm{MS}}$, where $c_{\mathrm{MS}} = \sqrt{\gamma p/\rho + B^2/4\pi\rho}$ is the magneto-sound velocity and $\Delta_{\min}$ is the highest spatial resolution of the nonuniform grid.

As far as the boundary conditions are concerned, we note that due to dissipative terms in resistive MHD the characteristics are not known at all [16]. Obviously, the same holds for the plasma-neutral gas–fluid equations. Thus, we do not know the mathematically well-posed boundary problem, but have to apply boundary conditions suggested by the physical problem under consideration. In our code symmetric and antisymmetric, as well as periodic, boundary conditions can be fixed according to the symmetry properties of the physical configuration. For the magnetic field $\nabla\cdot\mathbf{B} = 0$ is applied in order to avoid the severe problems associated with nonzero $\nabla\cdot\mathbf{B}$ caused by numerical errors [17]. In our numerical investigations on instability processes we usually choose the size of the system such that on the considered time scale the dynamical effects at the boundaries remain small. Thus, influences of the somewhat artificial boundary conditions on the dynamics of the simulated system are largely excluded.

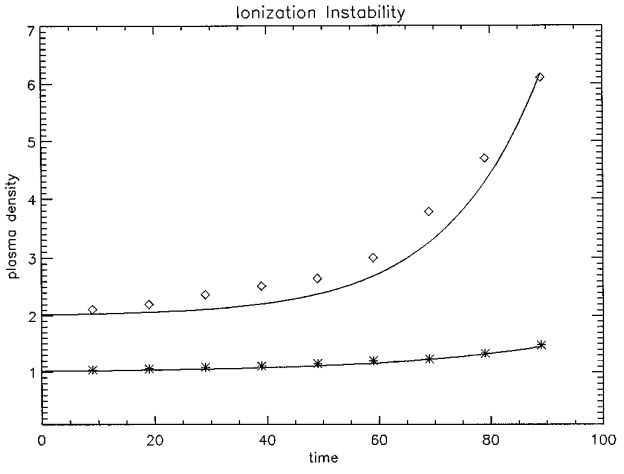

FIG. 1. The plasma mass density grows due to the ionization instability. The maximum mass density is plotted against the time for growth rates $q = 0.06$ (upper curve) and $q = 0.035$ (lower curve). Asterisks and diamonds represent the numerical results.

3. NUMERICAL TESTS

3.1. *Ionization Instability*

We consider a static and homogeneous plasma in ionization equilibrium. We choose the ionization frequency as $\iota(n) = \hat{\iota}n$ and a constant recombination coefficient $\beta = \hat{\beta}(\iota_0/\rho_0)$, where the index 0 denotes equilibrium quantities. If we assume incompressible perturbations of the form $\sim\exp(qt)$ the linearized plasma continuity equation reads

$$q\rho_1 = \iota_0\rho_1 + \iota_1\rho_0 - 2\beta\rho_0\rho_1. \qquad (48)$$

The growth rate q of the ionization instability is given by $q = (\hat{\iota} - \beta)n_0$, where we expanded $\iota_1 = (\partial\iota_0/\partial\rho_0)\rho_1$, assuming small perturbations in the ionization frequency.

Figure 1 shows the linear phase of the ionization instability. The solid curves show the analytically calculated temporal evolution of the maximum plasma mass density for normalized growth rates $q = 0.06$ (upper plot) and $q = 0.035$ (lower plot). The diamonds and asterisks give the numerical results. These results are gained for the equilib-

rium configuration characterized by $\hat{\imath} = 0.5$, $\rho_0 = 1$, and $\rho_0 = 2$, respectively. As is shown in Fig. 1 the code pretty well reproduces the analytical results of the linear dynamics of the ionization instability.

3.2. *Linear Wave Phenomena*

(a) *Damping of Alfven waves due to plasma–neutral gas friction.* In partially ionized gases Alfvén waves are damped by elastic collisions between neutrals and plasma particles. This effect can be calculated analytically with the help of the dispersion relation. We start from a static equilibrium with a homogeneous magnetic field. We assume ionization equilibrium and neglect the Hall term. Additionally, we neglect neutral gas motion in first order; i.e., we assume $\rho_n \gg \rho$. If we time differentiate the plasma equation of motion, after linearization we get

$$\rho_0 \frac{\partial^2 \mathbf{v}_1}{\partial t^2} = -\nabla \frac{\partial p_1}{\partial t} - \nu_{12}^S \frac{\partial \mathbf{v}_1}{\partial t} + \left(\nabla \times \frac{\partial \mathbf{B}_1}{\partial t}\right) \times \mathbf{B}_0. \quad (49)$$

The index 0 denotes equilibrium quantities, whereas the index 1 denotes perturbed ones. We suppose that the perturbed quantities are of the form

$$\mathbf{v}_1(\mathbf{x}, t) = \mathbf{v}_1 e^{i(\mathbf{kx}-\omega t)}, \quad \mathbf{B}_1(\mathbf{x}, t) = \mathbf{B}_1 e^{i(\mathbf{kx}-\omega t)}. \quad (50)$$

$\mathbf{k}$ is the wave vector and ω is the complex growth rate. The dispersion relation is found as

$$\omega^2 \mathbf{v}_1 = c_s^2 \mathbf{k}(\mathbf{k} \cdot \mathbf{v}_1) - i\omega \nu_{12}^S \mathbf{v}_1 + \frac{1}{\rho_0}[\mathbf{k} \times (\mathbf{k} \times (\mathbf{v}_1 \times \mathbf{B}_0)] \times \mathbf{B}_0. \quad (51)$$

If we assume that the equilibrium is dominated by the magnetic field (sound velocity $c_s \approx 0$) and assume incompressible perturbations ($\mathbf{k} \cdot \mathbf{v}_1 = 0$), we get

$$\frac{\omega^2}{v_A^2} \mathbf{v}_1 = -\frac{i\omega}{v_A^2} \nu_{12}^S \mathbf{v}_1 + k^2 \cos^2(\theta_B) \mathbf{v}_1 \quad (52)$$

with the solution

$$\omega = -\frac{i}{2} \rho_0 \nu_{12}^S \pm \sqrt{(k^2 \cos^2(\theta_B) v_A^2 - \nu_{12}^{S\,2})/4}; \quad (53)$$

v_A is the Alfvén velocity and θ_B is the angle between the wave vector and the magnetic field.

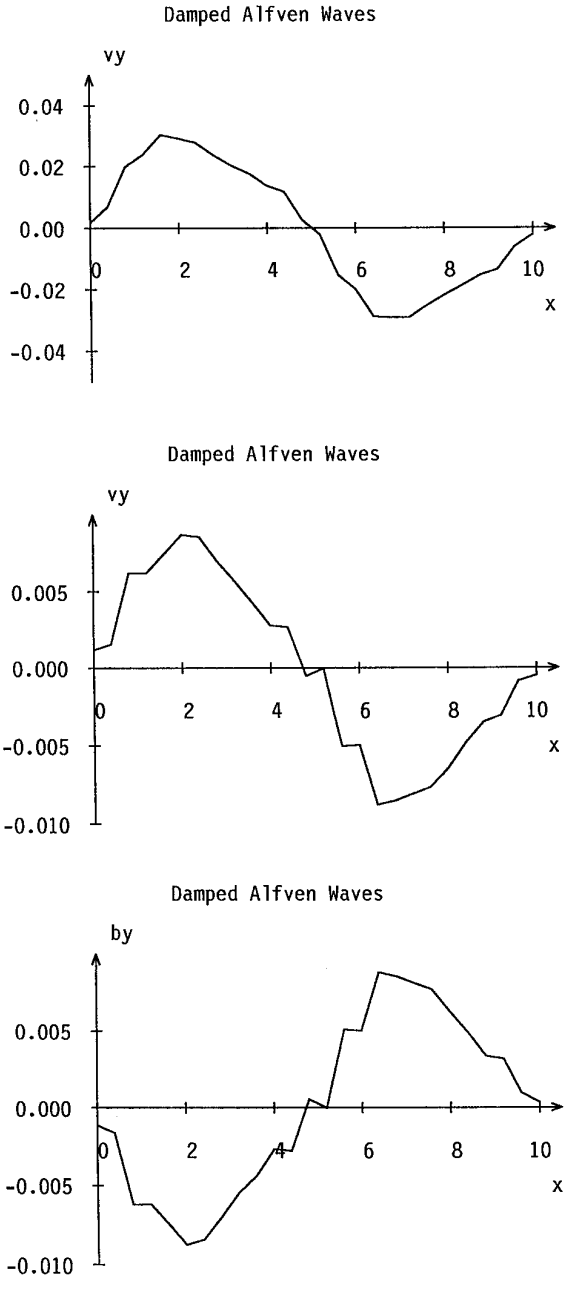

FIG. 2. Velocity (upper plots) and magnetic field (lower plot) of an Alfvén wave damped by plasma-neutral gas friction after 50 and 100 Alfvénic transit times.

Figure 2 shows results of the simulation of an Alfvén wave for $\nu_{12}^S = 0.05$, equal ion, and neutral masses, $\rho_n/\rho = 1000$, and $\cos(\theta_B) = 1$. The upper plots show the damping of the velocity amplitude after 50 and 100 Alfvénic transit times (τ_A), respectively. The lower plot shows the magnetic field amplitude after $100\tau_A$. The damping of the amplitudes, which are chosen as 0.1 at the beginning of the simulation, correspond to the results of the

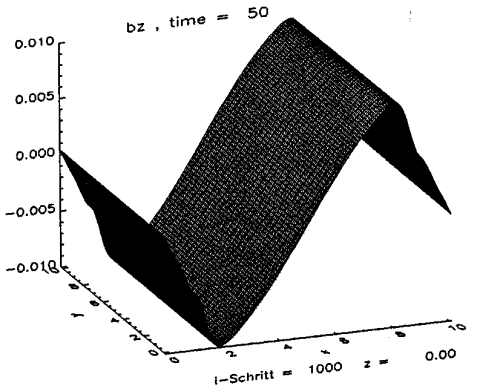

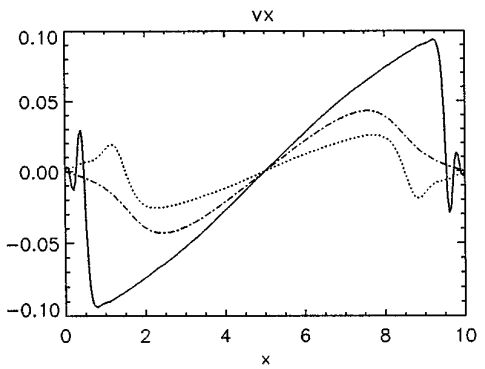

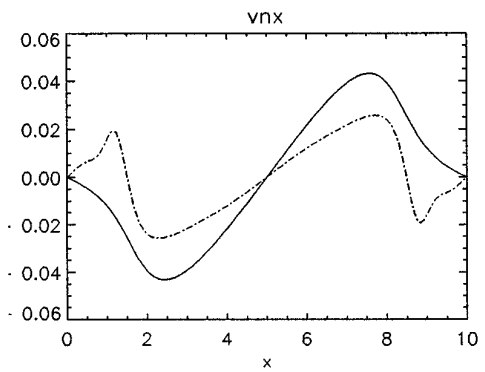

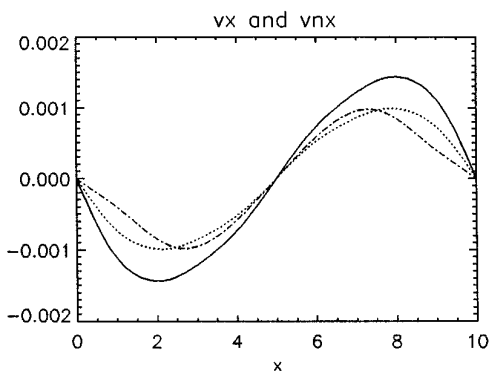

FIG. 3. Dynamics of a magnetosonic wave. The upper plot shows the perturbation magnetic field for $\rho = \rho_n$ and $\nu_{12}^S = 0.2$ after $50\tau_A$. The second plot shows v_x for $\rho = \nu_n$ and $\nu_{12}^S = 0.2$ after $25\tau_A$ (dashed line) and $50\tau_A$ (dotted line). The solid line indicates v_x after $75\tau_A$ in case of a totally ionized plasma. The third plot shows v_{n_x} for $\rho = \rho_n$ and $\nu_{12}^S = 0.2$ after $25\tau_A$ (solid line) and after $50\tau_A$ (dashed line). The bottom panel shows the wave damping for $\rho = 0.01\rho_n$ and $\nu_{12}^S = 0.1$. The solid line indicates v_x (the amplitude of the perturbation was again chosen as 0.1) and the dashed one indicates v_{n_x} after $60\tau_A$. After $80\tau_A$ the plasma and neutral gas velocities are similar and have the same phase (dashed line).

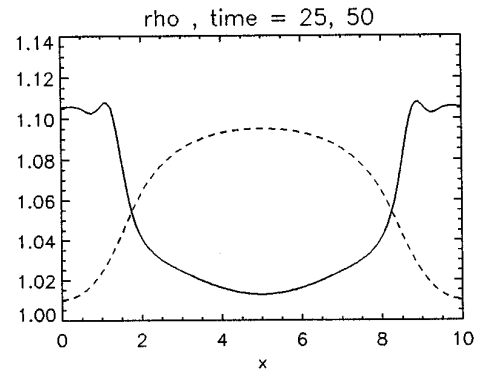

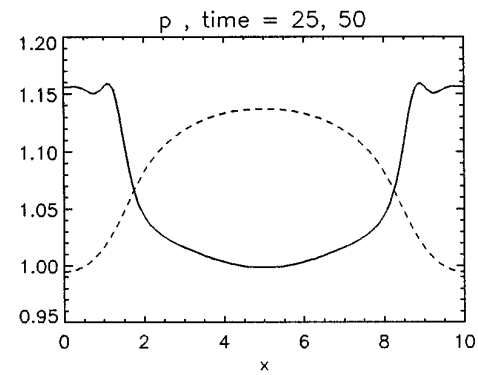

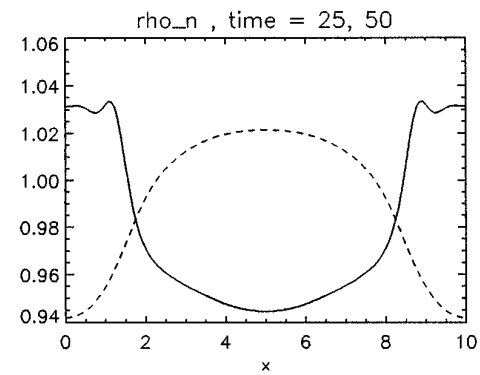

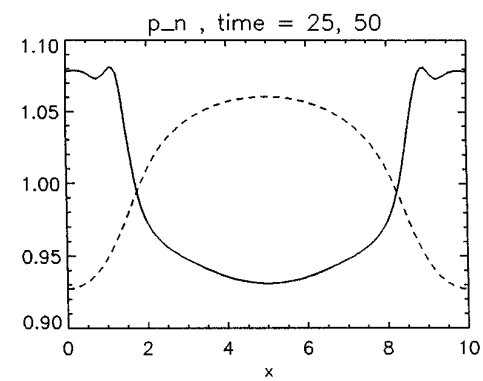

FIG. 4. Compression and depression of the plasma (upper plots) and neutral gas fluid (lower plots) due to the magnetisonic wave. The solid lines show mass densities (*rho* and *rho-n*) and thermal pressures (p and p-n) after $t = 25\tau_A$ and the dashed ones after $t = 50\tau_A$.

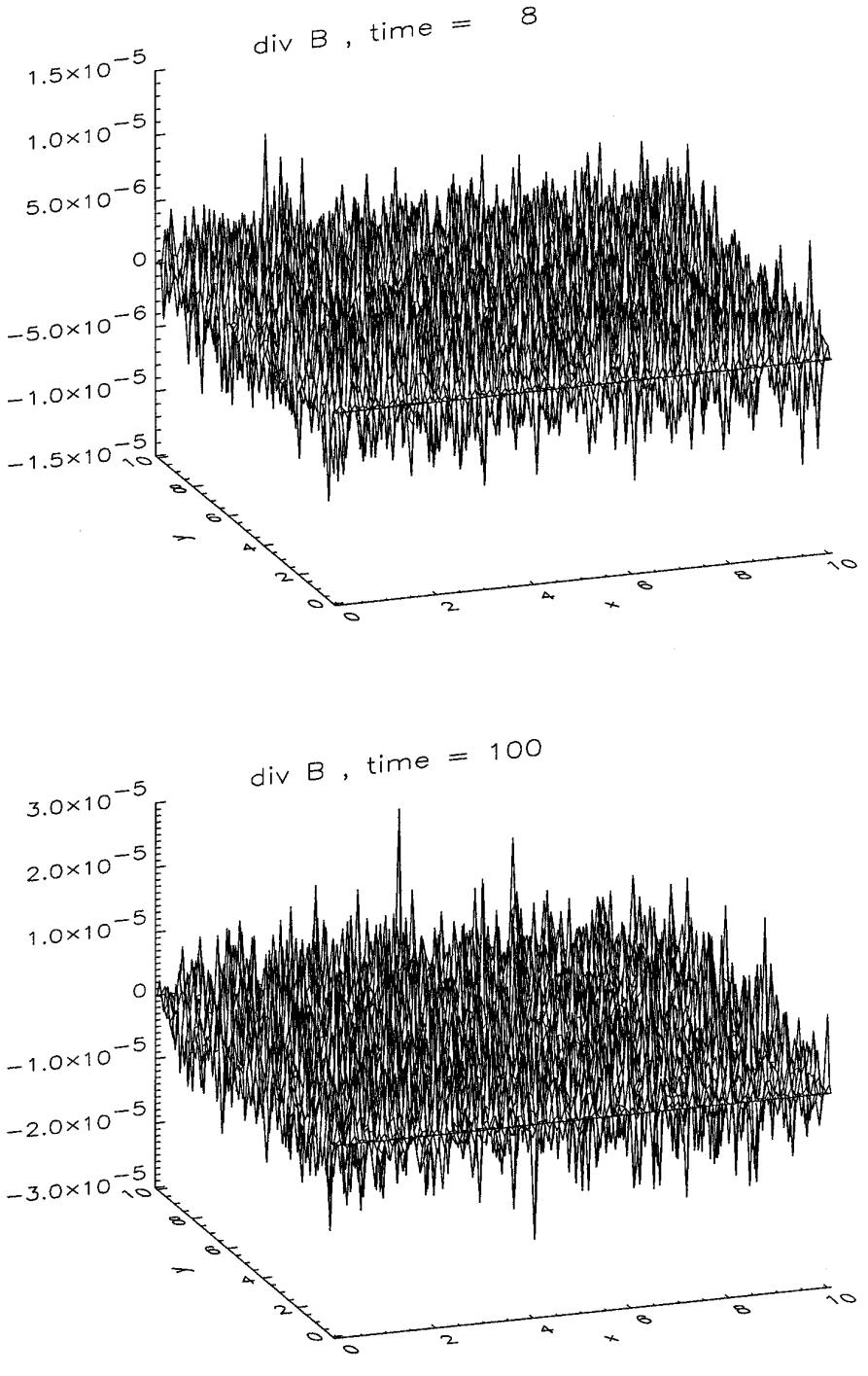

FIG. 5. Test of $\nabla \cdot \mathbf{B} = 0$ for the magnetosonic wave with $\rho = 0.01\rho_n$ and $\nu_{12}^S = 0.1$. The amplitude do not grow significantly with time and do not show any correlations.

analytic linear theory with 2% error after $50\tau_A$ and 5% after $100\tau_A$, respectively. We stress, that after 100 dynamic times neither numeric diffusion nor dispersion results in significant errors. The wave structure is rather well conserved.

(b) *Magnetosonic waves.* As Alfvén waves magnetosonic waves are damped in partially ionized plasmas. Starting with a homogeneous, isothermal plasma and a neutral gas fluid, a homogeneous magnetic field pointing in the x-direction and a velocity perturbation of $\mathbf{v} = 0.1\mathbf{e}_x$, the

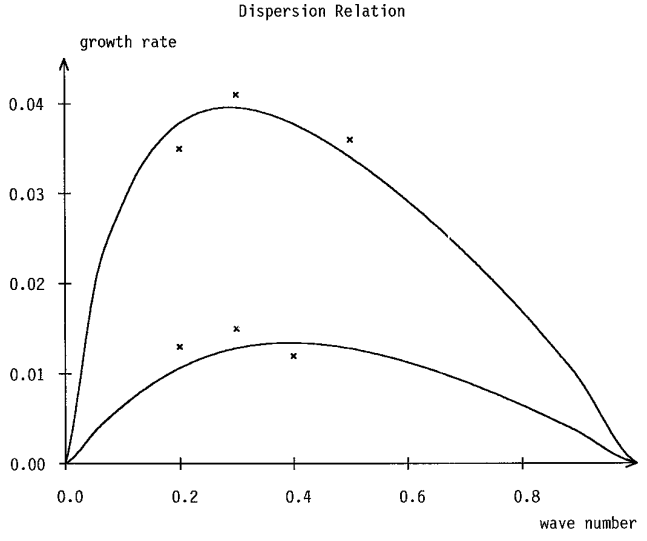

FIG. 6. The dispersion relation of the tearing mode in a partially ionized plasma ($\rho_n/\rho = 10000$). The magnetic Reynolds number is $S = 200$. The upper curve gives the dispersion relation for $\nu_{12S} = 0.005$ and the lower one for $\nu_{12S} = 0.5$. Crosses represent growth rates calculated by means of numerical simulations.

time development of the magnetosonic wave is illustrated in Fig. 3 and Fig. 4. The top panel in Fig. 3 shows the perturbation magnetic field for $\rho = \rho_n$ and $\nu_{12}^S = 0.2$ after $50\tau_A$. The second plot shows the damping of the wave for $\rho = \rho_n$ and $\nu_{12}^S = 0.2$ after 25 τ_A (dashed line) and $50\tau_A$ (dotted line). For comparison, the solid line indicates v_x after $75\tau_A$ when there is no plasma–neutral gas interaction ($\nu_{12}^S = 0$). The third plot shows the neutral gas dynamics caused by momentum transfer. The solid line represents the velocity for $\rho = \rho_n$ and $\nu_{12}^S = 0.2$ after $25\tau_A$ and the dashed one after $50\tau_A$. The bottom panel of Fig. 3 shows the wave damping for $\rho = 0.01\rho_n$ and $\nu_{12}^S = 0.1$. The solid line indicates the group velocity after $60\tau_A$ (the amplitude of the perturbation was again chosen as 0.1). The dashed line represents the associated neutral gas velocity. After $80\tau_A$ the plasma and neutral gas velocities are similar and both fluids oscillate with the same phase (dashed line). Magnetosonic waves are accompanied by plasma compression and depression. Figure 4 shows the temporal development (the equilibrium values for the mass densities as well as the pressures were chosen as 1.0) of the plasma mass density (*rho*), plasma thermal pressure (p), neutral gas mass density (*rho-n*) and neutral gas thermal pressure (p_n) after $25\tau_A$ (dotted lines) and $50\tau_A$ (solid lines), respectively. Again the wave structure is well conserved and the code reproduces well the expected features of magnetosonic wave damping.

A quite important test for the validity of a magnetohydrodynamic code is the strictness to which $\nabla \cdot \mathbf{B} = 0$ is satisfied. For illustration, in Fig. 5 we show the divergence of the magnetic field for the simulation of a magnetosonic wave for $\rho = 0.01\rho_n$. Note that, on the one hand, the amplitudes are rather small and do not grow significantly with time and, on the other hand, there is no systematic

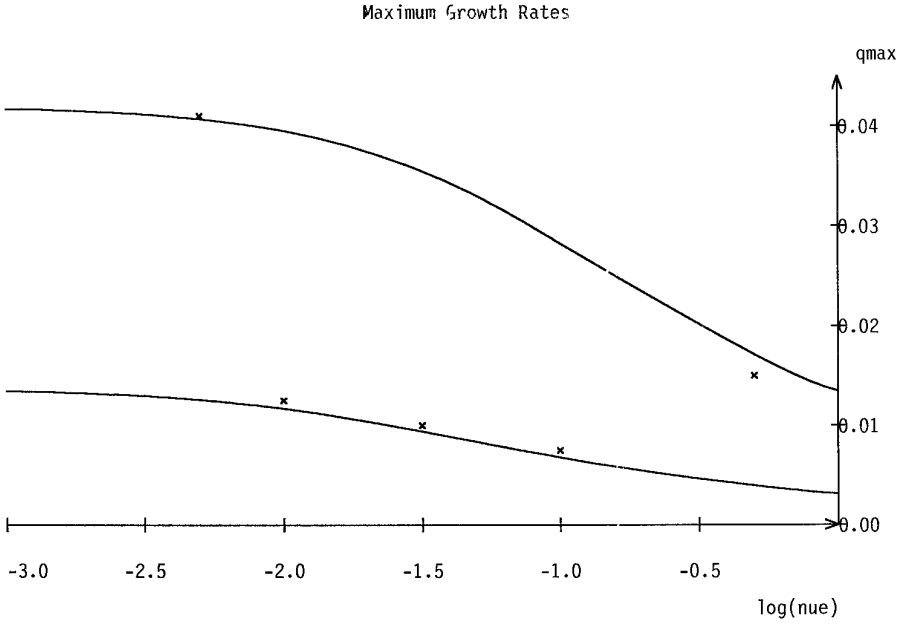

FIG. 7. Comparison of analytically calculated (solid curves) maximum growth rates (*qmax*) of the tearing instability in partially ionized plasmas with numerical results (represented by crosses). The growth rates are plotted against the logarithm of the effective collision frequency (ν_{12S}) for $S = 200$ (upper curve) and $S = 2000$ (lower curve).

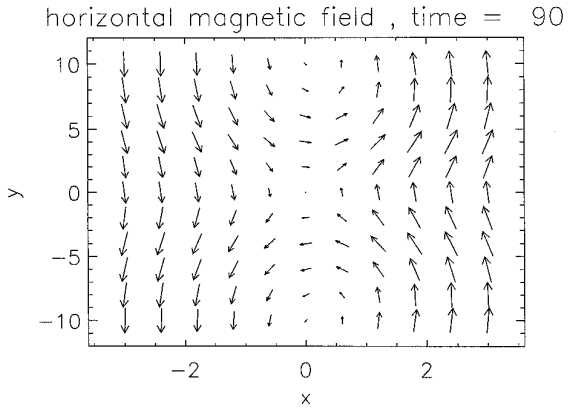

FIG. 8. The horizontal magnetic field at $z = 15$ after $90\tau_A$. The x-component of the magnetic field arises due the resistive instability.

violation of $\nabla \cdot \mathbf{B} = 0$. For the simulation of Alfvén waves and instabilities the results are similar, although the amplitudes of $\nabla \cdot \mathbf{B}$ grow up to $O(10^{-4})$. Additionally, we note that any violation of $\nabla \cdot \mathbf{B} = 0$ does not directly influence the integration of the plasma momentum equation, since we formulated the pressure force and the Lorentz force as the divergence of Maxwell's stress tensor, where we neglected the $\nabla \cdot \mathbf{B}$-term.

3.3. *Tearing Instability in Partially Ionized Gases*

The well-known tearing instability [18] plays an important role in laboratory and space plasmas. In partially ionized plasmas the growth rate of the mode is reduced due to plasma–neutral gas interaction [19–21]. For a wide range of parameters and different wave lengths of the mode the analytic dispersion relation can be reproduced by the code. We present results gained, starting from a one-dimensional static equilibrium.

$$\mathbf{B} = B_{y0}\tanh(x)\mathbf{e}_y + B_{z0}\mathbf{e}_z, \quad \rho = \rho_0, \quad p = p_0 + \cosh(x)^{-2}, \quad \rho_n = \rho_{n_0} = 10000\rho_0.$$

We assume thermal equilibrium between plasmas and neutral gas.

Figure 6 shows the analytic dispersion relation of the testing mode (cf. [21]). The magnetic Reynolds number was chosen as $S = 200$. The upper curve shows the dispersion relation for an effective collision frequency of $\nu_{12}^S = 0.005$, whereas the lower one shows the dispersion relation for $\nu_{12}^S = 0.5$. Crosses represent the normalized growth rates calculated by means of numerical simulations. Although we could not take into account small changes of the current profile due to nonlinear effects, the numerical results fit well to the analytical ones within numerical accuracy.

Figure 7 shows the maximum growth rates (*qmas*) for Reynolds numbers $S = 200$ (upper curve) and $S = 2000$ (lower curve) as functions of the effective collision frequencies ν_{12}^S in logarithmic representation. Again crosses represent the numerical results that also show good correspondence with the analytical ones.

3.4. *Nonlinear Dynamics of a Resistive Instability in the Upper Ionosphere*

In this section we present the non-linear development of the generalized tearing instability in a highly inhomogeneous configuration that can be used to model magnetosphere–ionosphere interaction processes. This resistive in-

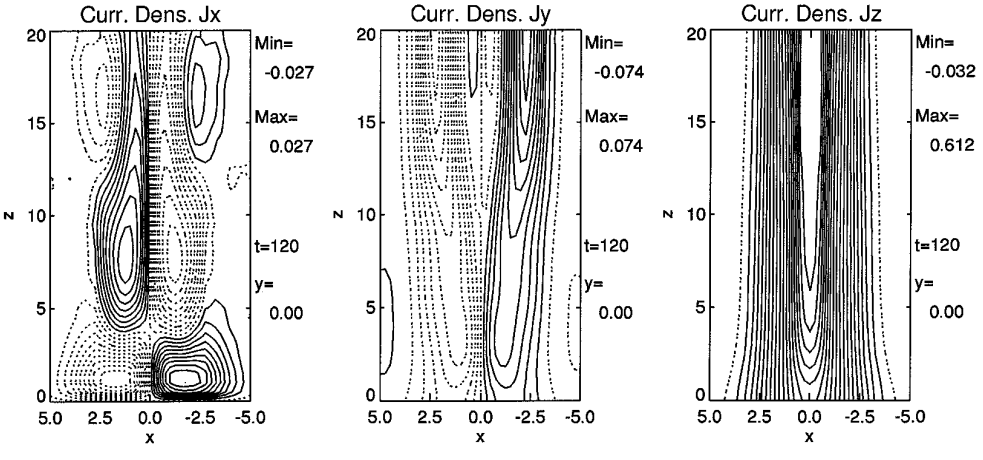

FIG. 9. The electric current density at $y = 0$ after $120\tau_A$. The diffusion of the current sheet (right plot) is due to the constant collisional resistivity (the initial current sheet thickness is 1 in normalized units). The complicated structure of j_x results from the combined diffusion and reconnection process (left plot). The y-component of the current density (middle plot) due the initial force-free magnetic field does not change significantly during the simulation.

stability can be regarded as a standard case for localized 3D reconnection processes [e.g., 22] that are believed to play a very important role in space and laboratory plasmas.

The initial configuration for modeling the resistive instability in the idealized ionosphere is characterized by a force-free magnetic field $\mathbf{B} = B_{y0}\tanh(x)\mathbf{e}_y - B_{z0}^2 + B_{y0}^2/\cosh(x)^2)^{1/2}\mathbf{e}_z$. We assume a static homogeneous plasma in thermal equilibrium with the neutral gas which is at rest. The altitude profile of the neutral gas density is given by the barometric formula. A constant collisional resistivity and effective plasma–neutral gas collision frequency ν_{12}^S are assumed to vary with the altitude, following the neutral gas density. At the upper boundary we apply sheared plasma flows ($v_y(x, z)$). These sheared flows with an amplitude of 10% of the Alfvén velocity lead to a further shear of the magnetic field and, thus, in an increase of the field-aligned electric current density. The principal idea is that if the current density exceeds a critical value, a localized region of anomalous resistivity will form at an altitude where the constant collisional resistivity due to electron–ion and ion–neutral collisions is negligible (the resistivity $\eta(j)$ is switched on) and, thus, the resistive instability will operate [cf. 23]. The results shown are received for typical ionospheric parameters. We have chosen line-symmetry at $y = 0$. The central reconnection region is located at $y = 0$ and $z = 15$.

Figure 8 shows the horizontal magnetic field at $z = 15$ $90\tau_A$ and after the onset of the resistive instability. The x-component of the magnetic field is caused by the reconnection process.

The components of the electric current density after $120\tau_A$ are shown in Fig. 9. The initial current sheet, with a thickness and an amplitude of 1 in normalized units, (j_z) has broadened due to diffusion, whereas the y-component of the current density, which is due to the initial force-free magnetic field configuration, has not changed significantly. The x-component of the current, which may contribute to ionospheric current closure in periodic current systems with alternating current directions, shows a more complicated structure. At lower altitudes the diffusion process due to the collisional resistivity dominates. The reversal in sign at higher altitudes is caused by the 3D instability process, which in the nonlinear stage results in a significant y-variation of the main component of the magnetic field.

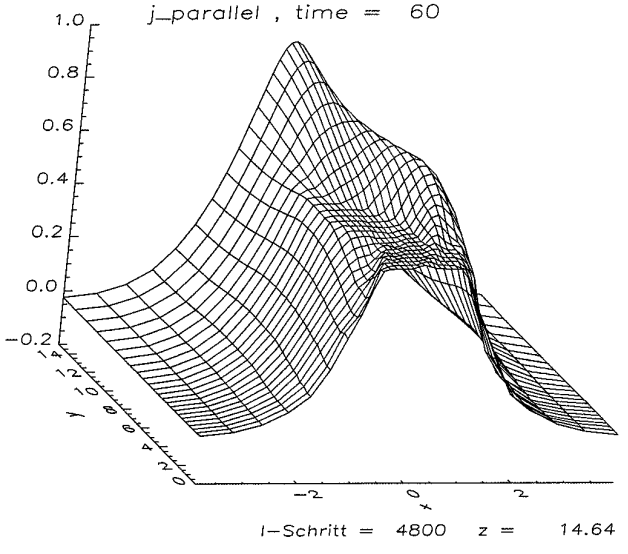

FIG. 10. The parallel current density after $60\tau_A$. The reduction of current density (the initial maximum was chosen as 1 in normalized units) due to the instability can be seen as well as the origin of a shock front in the positive x-half plane.

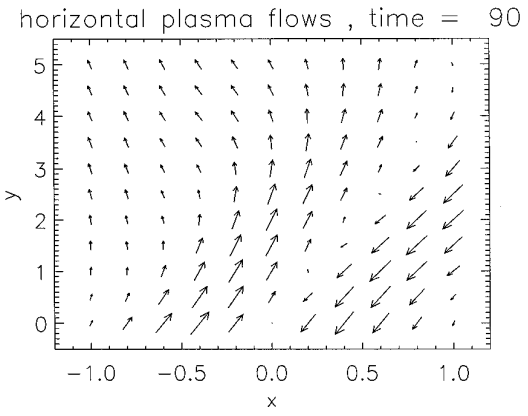

FIG. 11. Horizontal plasma flows caused by the resistive instability and the applied shear flows.

In Fig. 10 we show the parallel current density at $z = 15$ after $60\tau_A$. The reduction of current density due to the instability can be seen, as well as the origin of a slow mode or intermediate shock in the positive x-half plane, as is expected [cf. 24, 25]. This shock front cannot form as easily in the negative x-half-plane, because the sheared plasma flow at the upper boundary of the numerical box is transported down to the ionosphere via Alfvén waves and has the same direction as the divergent plasma flow due to the instability in the negative x-half-plane.

In Fig. 11 the plasma flows in the vicinity of the central reconnection region are shown. The strong flows are caused by the resistive instability [24, 25]. The shock forms, because the local Alfvén velocity is reduced due to plasma erosion in the reconnection region.

4. SUMMARY

We derived a set of balanced equations for plasma and neutral gas fluids. The code based on these equations allows for integrating the equations of mass and momentum densities, as well as of the pressures and of the magnetic field on a nonuniform spatial grid. The induction

equation includes electron pressure and the Hall term. To close the system of equations a dynamic equation for the electron pressure is taken into account, where we assumed that Ohmic dissipation directly results in heating of the electrons only. Within the limits of necessary assumptions and approximations mass density, momentum, and energy conservation are satisfied. The difference scheme is based on the leapfrog algorithm and was modified to include the source terms due to plasma–neutral gas interaction. The source terms of the fluid equations due to plasma–neutral gas interaction could be included without further restriction for the time step, in addition to the Courant–Friedrichs–Lewy condition. The validity of the code was proved by simulating characteristic linear and nonlinear plasma processes as wave and instability phenomena. Comparison of analytically calculated growth rates of the ionization instability as well as the tearing instability in partially ionized plasmas with the numerical results show good correspondence. Moreover, the analytical damping rate of Alfvén waves due to plasma–neutral gas friction could be verified numerically. Important applications for the presented code are the Earth's nonlinearly coupled ionosphere–thermosphere system, as well as the solar photosphere–chromosphere–corona system.

ACKNOWLEDGMENTS

This research was supported by the Deutsche Forschungsgemeinschaft (Bonn) through the Sonderforschungsbereich 191, "Physikalische Grundlagen der Niedertemperaturplasmen" and through Grant Schi156 17-1, by NATO (Brussels) Collaborative Research Grant SA.5-2-05(CRG.931368), by NSF Grant 91-11509, and by Department of Energy Grant DE-FG06-86ER 13530 to the University of Alaska Fairbanks.

REFERENCES

1. Y. Matsuda and J. J. Stewart, *J. Comput. Phys.* **66,** 197 (1986).
2. W. N. G. Hitchon, D. J. Koch, and J. B. Adams, *J. Comput. Phys.* **83,** 79 (1989).
3. E. L. Vold, F. Najmabadi, and R. W. Conn, *J. Comput. Phys.* **103,** 300 (1992).
4. G. Toth, *Astrophys. J.* **425,** 171 (1994).
5. J. D. Huba and J. A. Fedder, *Phys. Fluids B* **5,** 3779 (1994).
6. J. D. Huba, *Phys. Rev. Lett.* **72,** 2033 (1994).
7. D. E. Potter, *Computational Physics* (Wiley, London, 1973).
8. M. Mitchner and C. H. Kruger Jr., *Partially Ionized Gases* (Wiley, New York, 1973).
9. B. T. Draine, *Mon. Not. R. Astron. Soc.* **220,** 133 (1986).
10. A. Otto, *Comput. Phys. Commun.* **59,** 185 (1990).
11. A. Otto, K. Schindler, and J. Birn, *J. Geophys. Res.* **295,** 15023 (1990).
12. A. Otto, *Geophys. Astrophys. Fluid Dyn.* **62,** 69 (1991).
13. J. Birn and M. Hesse, *J. Geophys. Res.* **96,** 1611 (1991).
14. D. S. Harned and Z. Mikic, *J. Comput. Phys.* **83,** 1 (1989).
15. R. Courant, K. Friedrichs, and H. Lewy, *Math. Anal.* **100,** 32 (1928).
16. K. V. Roberts and D. E. Potter, "Magnetohydrodynamic Calculations," in *Methods in Computational Physics,* edited by B. Alder, S. Fernbach, and M. Rotenberg (Academic Press, New York, 1970), p. 340.
17. J. U. Brackbill and D. C. Barnes, *J. Comput. Phys.* **35,** 426 (1980).
18. H. P. Furth, J. Killeen, and M. N. Rosenbluth, *Phys. Fluids* **6,** 459 (1963).
19. R. B. Paris, *Plasma Phys.* **15,** 853 (1973).
20. E. G. Zweibel, *J. Geophys. Res.* **340,** 550 (1989).
21. A. Otto and G. T. Birk, *J. Geophys. Res.* **97,** 8391 (1992).
22. M. Hesse and K. Schindler, *J. Geophys. Res.* **93,** 5559 (1988).
23. A. Otto and G. T. Birk, *Geophys. Res. Lett.* **20,** 2833 (1993).
24. D. Biskamp, *Nonlinear Magnetohydrodynamics* (Cambridge Univ. Press, Cambridge, 1993).
25. A. L. LaBelle-Hamer, A. Otto, and L. C. Lee, *J. Geophys. Res.* **100,** 11875 (1995).